

Energy recovery modeling of pressure-retarded osmosis systems with membrane modules compatible with high salinity draw streams

Husnain Manzoor^a, Muaz A. Selam^a, Samer Adham^b, Ho Kyong Shon^c, Marcelo Castier^{a,d}, Ahmed Abdel-Wahab^{a,*}

^a Chemical Engineering Program, Texas A&M University at Qatar, P.O. Box 23874, Doha, Qatar

^b Global Water Sustainability Center, ConocoPhillips, P.O. Box 24750, Doha, Qatar

^c School of Civil and Environmental Engineering, University of Technology, Sydney, 15 Broadway, NSW 2007, Australia

^d Universidad Paraguayo Alemana, 1279 Lope de Vega, San Lorenzo, Paraguay



ARTICLE INFO

Keywords:

Pressure-retarded osmosis
Technoeconomic analysis
Produced water
Power density
Specific energy
Pareto optimality

ABSTRACT

A general framework for pressure-retarded osmosis (PRO) process simulation and optimization has been developed to generate *performance frontiers* (i.e. Pareto curves with respect to specific energy recovery vs. membrane power density) for a given process flowsheet – providing a basis for unequivocal comparisons to be made between the operability of various candidate membrane modules. This work confines itself to pairings between high-salinity oil-produced water (draw) and seawater (feed), which possess a high potential for osmotic energy recovery. It has been shown that the poor mass transfer behavior of a potential PRO membrane may significantly offset gains that could be realized from a high burst pressure compatible with the treatment of high-salinity draw streams. By applying suitable cost parameters to process optimization results and estimating resultant payback periods, it has been shown that the conventional PRO success criterion, which is based on a power density threshold of 5 W/m², is not sufficient to guarantee the feasibility of the membrane material in plant-scale operation – in the absence of additional optimization of the PRO process flowsheet.

1. Introduction

Pressure-retarded osmosis (PRO) processes present a potential mechanism for the utilization of hypersaline effluent waters for energy recovery. PRO, by pairing streams of relatively high salinity (draw) and relatively low salinity (feed) across a semipermeable membrane interface, takes advantage of the inherent osmotic potential which affects the permeation of water from the feed to the draw side. By design, the applied pressure to the draw stream is higher than that applied to the feed – while maintaining an applied pressure difference between the two streams which is less than their difference in osmotic pressure. The effect is to have an augmentation in volumetric flowrate of the draw stream – forming the basis for mechanical energy production (if the draw outlet is passed through a hydroturbine) or energy saving in a paired process e.g. coupling with seawater reverse osmosis (PRO-SWRO) through pressure exchanger networks.

The attractiveness of hypersaline draw streams (i.e. salinities in the range of 80–160 g/l) stems from their ubiquity as process effluents (e.g. hydrocarbon produced water or desalination brine), and the large theoretically recoverable energy from produced water-seawater

pairings (as calculated by the Gibbs free energy of mixing). However, a feasibility analysis of PRO processes of scale is hindered by the lack of a PRO unit simulation-optimization framework [1] which accounts for the effects of: 1) electrolyte solution non-ideality on the evaluation of osmotic driving force, 2) membrane non-ideality on the evaluation of permeate flux, 3) membrane pressure-drop, 4) continuous dilution of the draw stream over large membrane areas reducing the average driving force, and 5) pressure equipment inefficiencies. These phenomena significantly impact the magnitude of the net recoverable energy from a given PRO configuration. In general, the theoretical optimum applied hydraulic pressure (i.e., the applied pressure difference between the draw and feed streams) can be approximated as the half osmotic pressure difference ($\Delta P_{opt} \approx \Delta\pi/2$). For hypersaline draw streams paired with seawater, this optimum applied hydraulic pressure corresponds to 40–70 bar. Viably recovering energy from hypersaline water-seawater paired PRO configurations necessitates the use of PRO membrane modules with favorable mass transfer properties, and which can withstand such operating pressures (in the range of 40–70 bar). Having identified acceptable PRO membranes, process synthesis and process optimization must subsequently be introduced to specify PRO

* Corresponding author.

E-mail address: ahmed.wahab@qatar.tamu.edu (A. Abdel-Wahab).

<https://doi.org/10.1016/j.desal.2020.114624>

Received 21 April 2020; Received in revised form 7 July 2020; Accepted 13 July 2020

Available online 14 August 2020

0011-9164/© 2020 The Author(s). Published by Elsevier B.V. This is an open access article under the CC BY license (<http://creativecommons.org/licenses/by/4.0/>).

flowsheets (or SWRO-PRO flowsheets) and operating conditions which favor optimal net energy recovery sufficient in magnitude to justify the process itself. Insights gained from recent developments in membrane module synthesis and characterization, as well as simulation studies of plant-scale PRO processes, inform the approach of this work to the design of viable PRO processes.

Simulation and experimental studies have advocated the use of hypersaline draw streams, such as hydrocarbon-produced water, with the objective to offset energy consumption of the waterflooding operation. In one such study [2], commercial RO membranes with high burst pressures are simulated in PRO mode – demonstrating that energy recovery is severely inhibited by external concentration polarization (ECP) and internal concentration polarization (ICP) associated with the high structural parameter of these membranes. Relatively poor mass transfer behavior of high-pressure membranes has also been observed by Madsen et al. [3], who perform a comprehensive experimental screening of commercially available FO membranes operated in PRO mode. They show that the structural parameter of a given membrane module increases with applied pressure – implying that poor mass transfer behavior is a phenomenon intrinsic not just to high burst pressure membranes, but to high-pressure operation itself. Madsen et al. also note, however, that sensitivity of the structural parameter to applied pressure differs from membrane to membrane. This provides a basis for optimizing the staged operation of different types of membrane modules within the same process flowsheet – each operating at a distinct pressure.

With respect to non-commercial PRO membranes, Straub et al. [4] have fabricated modules suitable for operation up to 48 bar – with observed power densities in the order of 60 W/m² for a 3 M NaCl draw stream paired with deionized water. The operability of this membrane module at pressures commensurate with the osmotic pressure of high salinity produced water would imply the favorability of its use in energy recovery from hypersaline draw solutions paired with seawater, seawater brine, or brackish water feed solutions. The feasibility of such processes can best be evaluated through the deployment of process simulators.

Plant-scale simulations enable an accurate determination of the scalability of PRO membranes demonstrated at the coupon-scale for RO brine paired with seawater as reported by Kim et al. [5], with a methodology for the optimization of operating conditions for various process flowsheets. Simulation studies on plant-scale PRO processes include that of Yang et al. [6], in which maximum membrane areas are calculated such that the draw and feed streams reach equilibrium (i.e. $\Delta P = \Delta \pi$), while utilizing a finite element iterative approach to solve for countercurrent flows in a membrane module. In the context of process optimization studies, Long et al. [7] introduced energy efficiency – defined as the percentage of the Gibbs free energy of mixing recovered by the process. In our previous work [8], plant-scale PRO simulations were based upon the application of an equation of state for electrolyte solutions to enable reliable predictions of osmotic pressure differences across PRO modules.

Process simulation has also demonstrated the benefits of staging such that the operating parameters of each staged unit are optimized for the extent of dilution at that particular stage. Sotani and Struchtrup [9] reported various dual stage configurations (while accounting for irreversible losses) – reporting gains in specific energy recovery of up to 8% relative to the corresponding single stage process that was simulated.

SWRO-PRO hybrid systems maneuver around the challenge of low turbine efficiencies by inducing energy savings in RO, rather than energy production from PRO. This derives from the inherently higher efficiency of pressure exchangers relative to turbines/pumps. Optimization studies of Touati et al. [10] on SWRO-PRO hybrid systems reported energy savings in RO (relative to the isolated RO process) in the range of 12%-18%.

This study seeks to identify the viability of existing PRO membranes, and their corresponding optimal operating conditions, such that

they feasibly recover energy from high salinity hydrocarbon-produced water as a result of energy production (draw outlet passed through hydroturbine). Our analysis is restricted to membrane modules which have been demonstrated in the literature to withstand applied hydraulic pressures in the range of 40-70 bar – commensurate with the use of high salinity draw streams. PRO configurations are modeled with an in-house simulator – based on the use of an electrolyte equation of state (EoS) and incorporating all performance-limiting phenomena – including internal/external concentration polarization, and the effect of reverse salt flux.

2. Methodology

The developed simulator models the performance of flowsheets consisting of user-specified configurations of pumps, turbines, pressure exchangers and membrane modules. Stream property calculations, which feed into the equipment models, are carried out with the Q-electrolattice equation of state (EoS) developed by Zuber et al. [11]. Use of an advanced electrolyte EoS enables the accurate calculation of solution thermodynamic properties as a function of temperature, pressure and composition. Accurate evaluation of the osmotic pressure differences between feed and draw streams (which drives the osmotic process) enables reliable predictions of energy recovery from the PRO unit. Details about the simulator and its models and methods were presented in our previous publication [8]; herein we provide a summary of its main features.

2.1. Thermodynamic modeling

The Q-electrolattice [11] EoS is employed, which is based on a Helmholtz free energy expansion. All thermodynamic properties are obtained from this function using relationships of classical thermodynamics. The properties of interest are the density, molar enthalpy, and molar entropy of the process streams and the chemical potential of water, which is used in the evaluation of the osmotic pressure. The residual Helmholtz free energy in the Q-Electrolattice EoS is given by:

$$A^R(T, V, n) = \Delta A^{MTC} + \Delta A^{Born} + \Delta A^{MSA} \quad (1)$$

where ΔA^{MTC} represents the contribution due to short-range non-electrostatic interactions to the Helmholtz free energy based on the Matted-Tavares-Castier (MTC) EoS [12]. ΔA^{Born} represents the contribution due to ion solvation effects based on Born model [13] and ΔA^{MSA} represents the contribution due to long-range ion-ion interactions based on Mean Spherical Approximation [14]. The mathematical expressions for these three contributions are available in the original reference for the Q-electrolattice EoS [11].

To calculate the real enthalpies and entropies of the solution, ideal gas properties of the solution are calculated and added to the residual properties generated by the Q-electrolattice EoS, at the same temperature and pressure. The osmotic pressure predictions are also obtained from the Q-electrolattice EoS. An electrolyte solution separated by a semi-permeable membrane from a pure solvent, maintained at the same temperature will reach equilibrium when the pressure difference is such that there is no flow of solvent from pure solvent side to the solution side. Based on this definition, the fugacity of the solvent in the solution and of the pure solvent at the equilibrium are given by:

$$f_s^I = f_s^{II} \quad (2)$$

where f_s^I and f_s^{II} are the fugacity of the solvent in the solution and pure solvent at the same temperature, respectively. Eq. (2), when written in terms of its variables, results in:

$$x_s^I \varphi_s^I \left(T_s, P_s^I, x^I \right) P_s^I = x_s^{II} \varphi_s^{II} \left(T_s, P_s^{II}, x^{II} \right) P_s^{II} \quad (3)$$

where φ_s^I and φ_s^{II} are the fugacity coefficients of the solvent in the solution and pure solvent, respectively, x^I and x^{II} are the mole fractions in the solution and in the pure solvent. For the purpose of our calculation, the pressure of the pure solvent is chosen to be 1 atm and Eq. (3) is then solved for P_s^I such that the equilibrium condition is satisfied. Hence, the osmotic pressure of the solution, π , in reference to the pure solvent conditions, after the equilibrium condition is satisfied, is given by:

$$\pi = P_s^I - P_s^{II} \quad (4)$$

2.2. Equipment modeling

The main computational modules in the simulator are for pumps, turbines, pressure exchangers, and membrane units, whose features are presented in this section. The simulator also contains ancillary modules, such as those for stream mixers and splitters and for the numerical convergence of iterative calculations.

2.2.1. Pumps and turbines

The first law of thermodynamics, under the assumptions of adiabatic and steady state operation and neglecting changes to the fluid's kinetic and potential energies, gives that the shaft power (\dot{W}_{shaft}) in these pieces of equipment is:

$$\dot{W}_{shaft} = \dot{n} \left(h_{out} \left(T_{out}, P_{out}, x_{-out} \right) - h_{in} \left(T_{in}, P_{in}, x_{-in} \right) \right) \quad (5)$$

where h and x represent the molar enthalpy and component mole fractions, respectively. The subscripts *in* and *out* indicate whether the property corresponds to the unit inlet or outlet. The model assumes that the molar flowrate, represented by \dot{n} , and the component mole fractions remain unchanged across each pump or turbine.

For a specified outlet pressure, the a first approximation to the outlet temperature is obtained under the assumption of isentropic operation, that is:

$$\dot{n} \left(s_{out} \left(T_{out}, P_{out}, x_{-out} \right) - s_{in} \left(T_{in}, P_{in}, x_{-in} \right) \right) = 0 \quad (6)$$

where s is the molar entropy. The adiabatic and reversible shaft power, $\dot{W}_{shaft,rev}$, is calculated by substituting the evaluated outlet stream temperature into Eq. (5). The assumption of reversibility is then relaxed to enable user-specified efficiencies (η). For a pump,

$$\dot{W}_{shaft} = \frac{\dot{W}_{shaft,rev}}{\eta_{pump}} \quad (7)$$

For a turbine,

$$\dot{W}_{shaft} = \eta_{turbine} \dot{W}_{shaft,rev} \quad (8)$$

In either case, pump or turbine, the outlet stream temperature is then re-evaluated numerically such that it satisfies the energy balance given by Eq. (5).

2.2.2. Pressure exchangers

Pressure exchangers transfer mechanical energy from a high-pressure fluid to a low-pressure fluid by interfacing both streams across a single unit. Energy is transferred from the depressurization to the pressurization section of the pressure exchanger. Fig. 1 displays a schematic of a pressure exchanger.

The depressurization side of pressure exchanger is modeled in a similar manner to that of a turbine, where the outlet pressure and thermodynamic efficiency of this section is specified by the user. As described previously for pumps and turbines, the calculation is initiated assuming adiabatic and reversible operation, with isentropic power ($\dot{W}_{HP,rev}$) and temperatures evaluated from Eqs. (5) and (6). The real

power transferred from the depressurization, \dot{W}_{HP} , is then evaluated using Eq. (8) and substituted in Eq. (5) to satisfy the energy balance by re-evaluating the temperature of the outlet stream.

For the pressurization side, the output pressure is unknown and must be determined from the power supplied by the depressurization side - \dot{W}_{HP} . It is assumed that a portion of this power is used to compress the fluid on the pressurization side with a thermodynamic efficiency η_{LP} . The portion $(1 - \eta_{LP})\dot{W}_{HP}$ is assumed to be dissipated as heat due to frictional losses on the pressurization side, resulting in entropy generation. The entropy balance for the pressurization is given by:

$$\dot{n}_{LP} (s_{LP,in} - s_{LP,out}) + \dot{S}_{gen} = 0 \quad (9)$$

where \dot{n}_{LP} is the molar flowrate of the low-pressure stream and \dot{S}_{gen} is the rate of entropy generation, which is given by:

$$\dot{S}_{gen} = \frac{\dot{Q}}{T} \quad (10)$$

where

$$\dot{Q} = (1 - \eta_{LP}) \times |\dot{W}_{HP}| \quad (11)$$

T in Eq. (10) is taken as the arithmetic average temperature of the inlet and outlet streams on the pressurization side of the pressure exchanger and \dot{Q} is the heat generation rate.

In summary, while referring to Fig. 1, the energy and entropy balances applied to the pressurization side of the pressure exchanger are:

$$\dot{n}_{LP} h \left(T_{LP,out}, P_{LP,out}, x_{-LP} \right) = \dot{n}_{LP} h \left(T_{LP,in}, P_{LP,in}, x_{-LP} \right) + |\dot{W}_{HP}| \quad (12)$$

$$\dot{n}_{LP} s \left(T_{LP,out}, P_{LP,out}, x_{-LP} \right) = \dot{n}_{LP} s \left(T_{LP,in}, P_{LP,in}, x_{-LP} \right) + \frac{(1 - \eta_{LP}) \times |\dot{W}_{HP}|}{(T_{LP,in} + T_{LP,out})/2} \quad (13)$$

These simultaneous numerical solution of these two equations provides the values of $T_{LP, out}$ and $P_{LP, out}$.

2.2.3. Membrane modules

Bench scale calculations can safely ignore variations in stream properties along the membrane due to the small membrane areas. This assumption fails for a plant-scale module due to the large rate of permeation across the relatively larger membrane - causing significant dilution of the draw stream and corresponding concentration of feed stream. Variations in stream properties along the membrane must be accounted for in evaluating its performance. In the developed simulator, the membrane is discretized using finite differences to integrate flux along the membrane area. Membrane discretization is illustrated in Fig. 2; each discrete element is solved ensuring that the overall boundary conditions are satisfied. The following assumptions are made to model the membrane unit:

- Perfect mixing at each discrete membrane element;
- Isothermal operation. i.e. the outlet temperatures of the draw and feed streams are the same as their respective inlet streams; and
- User-specified pressure drop for the membrane unit. The magnitude of the total pressure drop is distributed linearly across the membrane.

In Fig. 2, D represents the draw side of the membrane and F represents the feed side. For all of the various process configurations studied in this work, draw and feed streams were modeled as flowing counter-current to one another. Counter-current operation of PRO units has been consistently shown to result in higher power output relative to co-current flow (as discussed by Zwan et al. [15]).

The following mass balance equations are solved at each discrete element 'j' of the membrane module:

Draw stream (D):

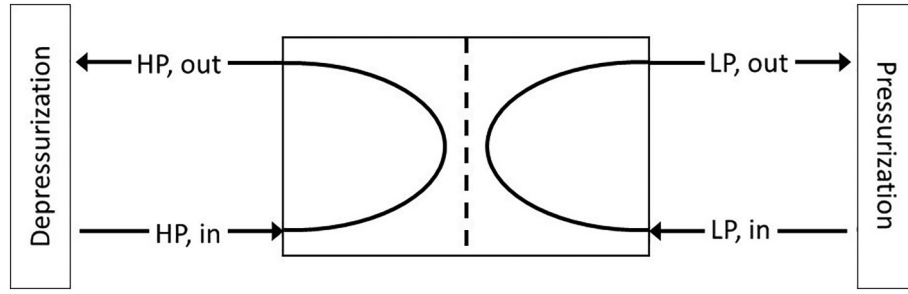


Fig. 1. Schematic of a Pressure exchanger.

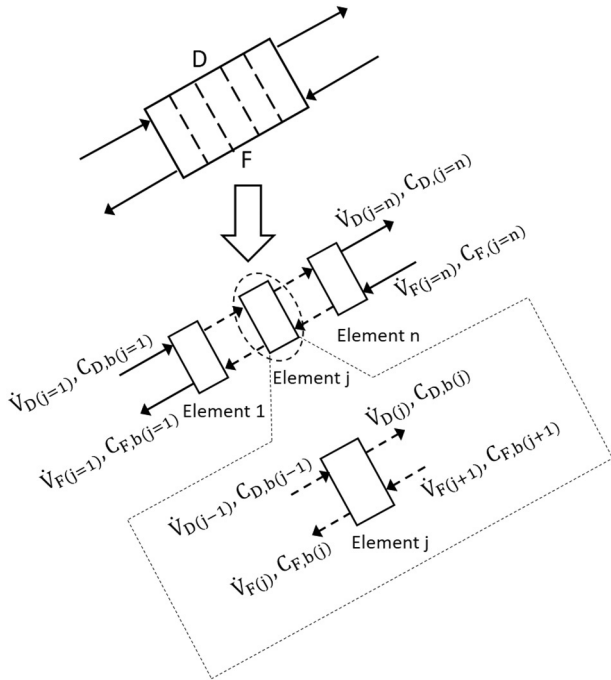


Fig. 2. Elaborated discretization of a counter-current membrane module.

$$n_{w,j-1}^D + J_{w,j} = n_{w,j}^D \quad (14)$$

$$n_{s,j-1}^D - J_{s,j} = n_{s,j}^D \quad (15)$$

Feed stream (F):

$$n_{w,j+1}^F - J_{w,j} = n_{w,j}^F \quad (16)$$

$$n_{s,j+1}^F + J_{s,j} = n_{s,j}^F \quad (17)$$

where n_i^D and n_i^F are molar flowrate of species i – solute (s) or water (w) – in the draw and feed streams.

Treatment of the fluxes in the membrane module is based upon the mass transfer model published by Yip et al. [16]. This model accounts for the performance-limiting phenomena of internal concentration polarization, external concentration polarization and reverse salt permeation to predict the fluxes across the membrane. Water permeate flux in PRO mode, based on this mass transfer model, is calculated from Eq. (18):

$$J_w = A \left[\frac{\pi_{D,b} \exp\left(-\frac{J_w}{k}\right) - \pi_{F,b} \exp\left(\frac{J_w}{D}\right)}{1 + \frac{B}{J_w} \left\{ \exp\left(\frac{J_w}{D}\right) - \exp\left(-\frac{J_w}{k}\right) \right\}} - \Delta P \right] \quad (18)$$

where, A , S , k are the water permeability coefficient, structural parameter and mass transfer coefficient of the membrane, respectively. $\pi_{D,b}$ and $\pi_{F,b}$ are the bulk osmotic draw and feed pressures, respectively.

The reverse solute flux is given by:

$$J_s = B \left[\frac{C_{D,b} \exp\left(-\frac{J_w}{k}\right) - C_{F,b} \exp\left(\frac{J_w}{D}\right)}{1 + \frac{B}{J_w} \left\{ \exp\left(\frac{J_w}{D}\right) - \exp\left(-\frac{J_w}{k}\right) \right\}} \right] \quad (19)$$

where, B , $C_{F,b}$, and $C_{D,b}$ are the salt permeability coefficient, the bulk feed solute concentration, and the bulk draw solute concentration, respectively.

Eqs. (18) and (19) evaluate the water and reverse solute flux at any finite element of the membrane interface, such that cumulative dilution and concentration effects (and their diminishing effect on net-driving force) is accurately accounted for when evaluating the performance of the membrane.

The membrane module automates the incorporation of pressure drop along the membrane on both the draw and feed sides. The pressure drop correlation, which originates from the First Law equation (Simplified Bernoulli's equation [17]) is given by:

$$\Delta P_{Drop} = \left(\frac{\dot{V}}{\dot{V}_{ref}} \right)^2 P_{ref} \quad (20)$$

where, \dot{V} represents the volumetric flowrate on the draw side, and \dot{V}_{ref} represents a reference maximum flowrate for the given membrane. Due to lack of available pressure drop data specifically for commercial PRO membranes, reference pressure drop values are assumed based on the experimentally-determined ratings of representative RO [18] and PRO [19] modules. The feed side maximum pressure drop is taken to be 0.6 bar ($P_{ref, feed}$) – corresponding to a maximum flowrate of 17 m³/h ($\dot{V}_{ref, feed}$) [18], while the draw side maximum pressure drop is set at 0.16 bar ($P_{ref, draw}$) at a maximum allowable draw flowrate of 4.4 m³/h ($\dot{V}_{ref, draw}$) [19]. It should be observed that the pressure drop ratings quantified above are reference values to be substituted in Eq. (20) as an input to calculate the actual pressure drop in the module as a function of volumetric flowrate. The objective of this pressure drop formulation is for the simulator to generate pressure drop values of the correct order of magnitude for an adequate feasibility analysis, and which vary with volumetric flowrate according to the correct functionality (as determined by Eq. (20)). More precise treatments would account for the length of the membrane flow channel and number of modules [9].

2.3. Membrane selection

This computational work focuses primarily on the feasibility of high salinity solution pairings. Oil-produced water (2.73 M NaCl, $\pi = 155$ bar) is specified as the draw solution input, while seawater (0.6 M NaCl, $\pi = 27.6$ bar) is assumed as the feed solution in all cases. Osmotic pressures corresponding to specified salinities have been evaluated by the thermodynamic model embedded in the simulator (the Q-electrolattice EoS) [8].

It can be taken as a general rule that the optimum applied hydraulic pressure difference between the feed and draw streams lies in the vicinity of $\Delta\pi/2$ [20]. Since the optimum applied hydraulic pressure

difference between oil-produced water and seawater ($\Delta\pi/2 \approx 63.7$ bar) is relatively high, it is only reasonable to include in this computational study membranes (or membrane modules) which have demonstrated, at least at a lab scale, the ability to withstand operating pressures in these ranges.

Among the membranes which have demonstrated high-pressure operation, Straub et al. [4] report operating pressures for their developed PRO test cell of up to 48 bar. This was accomplished by loading commercial flat-sheet, thin-film composite (TFC) forward osmosis (FO) membranes onto a custom-built support structure compatible with high pressure operation. Madsen et al. [3] have studied the mechanical stability of various commercially available forward osmosis membranes – specifically with respect to their applicability to hypersaline solutions. They have reported that the use of a sintered stainless-steel plate as a feed channel spacer enables the membrane cell to withstand pressures up to 70 bar. This modification, though resulting in severe internal concentration polarization and hindered flux (due to lower effective flowrates), enables the system to fully utilize the osmotic potential of high salinity solutions. Membrane characteristic parameters reported by Straub et al. [4] and Madsen et al. [3] are taken as inputs to the simulation of full-scale modules treating the oil-produced water (draw) and seawater (feed) system.

Gonzales et al. [21] also reported properties of a commercial PRO membrane manufactured by Toray Inc. Although the membrane reported is able to withstand limited pressures of up to 27 bar, this membrane has also been included in our study to provide an indication of the feasibility of existing commercial PRO membranes. The characteristic parameters of membranes modeled in this work are compiled in Table 1. Madsen et al. [3] have also conducted experimental runs on commercially available Aquaporin membranes without providing the characteristic membrane parameters (A, B, S) essential for the simulation of power density curves. Moreover, the maximum operating pressure of a representative aquaporin membrane (as demonstrated by Madsen et al. [3]) is 10 bar – which is well below the optimal applied pressure difference for produced water-seawater pairings. Therefore, aquaporin membranes were excluded from this study.

2.4. Optimization methodology

This work explores the effect of membrane area, operating pressure and inlet feed/draw flowrates on the membrane power density and specific energy of the process. A suitable value or range of values is specified to define the optimization space. The optimization itself is executed using the Multi-objective Genetic Algorithm built into the Dakota tool [22]. These type of optimization methods are especially useful for conflicting objective functions (in this case membrane power density vs. overall plant specific energy recovery). This method generates a Pareto optimal solution sets (i.e. nondominated with respect to the two objective functions) isolated from the entire solution space. This multi-objective genetic algorithm method is especially appropriate since it precludes the need for the collection and scaling of objective function values to transform them into a single objective.

Optimization of the PRO process necessitates a precise definition of objective functions. The objective functions chosen for the optimization

process were the power density of the membrane and specific energy applicable to the plant as a whole - defined by Eqs. (21) and (22), respectively.

$$\overline{PD} = \frac{\Delta \dot{V}_{water} \Delta P}{A_m} \tag{21}$$

$$SE = \frac{|\sum \dot{W}|}{\dot{V}_F + \dot{V}_D} = \frac{|\dot{W}_{Pump} + \dot{W}_{Turbine} + \dot{W}_{PXLoss} + \dot{W}_{PWTreatment} + \dot{W}_{SWTreatment} + \dot{W}_{\Delta PDrop}|}{\dot{V}_F + \dot{V}_D} \tag{22}$$

where, in Eq. (21), \overline{PD} is the average power density of the membrane module, ΔP is the applied hydraulic pressure difference, $\Delta \dot{V}_{water}$ is the rate of water permeation and A_m is the total membrane area of a module. In Eq. (22), $\dot{W}_{Turbine}$ is the power generation from the turbine. Consistently with the sign convention adopted for the energy balance in Eq. (4), $\dot{W}_{Turbine}$ is a negative number. The other terms on the numerator of the right hand side of Eq. (22) are all positive: \dot{W}_{Pump} is the power input to the pump, $\dot{W}_{Turbine}$ is the power generation from the turbine. Consistently with the sign convention adopted for the energy balance in Eq. (4), $\dot{W}_{Turbine}$ is a negative number. The other terms on the numerator of the right hand side of Eq. (22) are all positive: \dot{W}_{PXLoss} is the power lost in the pressure exchanger (originating from a user-specified inefficiency), $\dot{W}_{PWTreatment}$ and $\dot{W}_{SWTreatment}$ represent the power used in the pretreatment of produced water and seawater, respectively, and $\dot{W}_{\Delta PDrop}$ is the power lost due to pressure drop in the membrane module. Altogether, the numerator in Eq. (22) represents the net mechanical power that the PRO process delivers. Finally, \dot{V}_F and \dot{V}_D are the volumetric feed and draw flowrates entering the membrane module, respectively.

These objective functions have been designed to capture the tradeoff between power output per square meter of membrane area, and the total power output from the plant as a whole. The phenomenon of draw stream dilution along the area of the membrane emerges at the module-scale – reducing the average osmotic driving force in the membrane and, by extension, the average power density. This is captured by Eq. (21), and can be taken as an indication of the return per square unit membrane area invested in the process. Eq. (22) represents the specific energy recovered (per unit total volumetric flowrate draw and feed streams entering the process) – for the given conditions at which the plant is operating. The chosen definition for specific energy recovery reflects energy losses which result from the inefficiencies of various equipment within the plant, the pretreatment process and the pressure drop along the membrane module. Larger module areas, while enabling greater power output from the process as a whole (specific energy), engender diminishing marginal returns per square unit membrane area introduced to the module (average power density). This definition of specific energy bears a direct relationship to the inlet volumetric flowrates of the feed and draw streams, which are a subset of the optimized process parameters (along with the membrane area and the operating pressure, as discussed in Section 3.2). This translates to the identification of optimal combinations of feed and draw flowrates which maximize the energy recovered per unit total process stream flowrate. In order to estimate the energetic costs associated with

Table 1
Membrane properties as reported by Madsen et al. [3], Straub et al. [4], and Gonzales et al. [21].

Source	Straub et al.	Madsen et al.	Madsen et al.	Gonzales et al.
Membrane type	HTI-TFC	FTS-CTA	HTI-CTA	Toray-TFC
Membrane	1	2	3	4
A, Water permeability, (L/m ² .h.bar)	2.49	0.69	0.42	1.23
B, Salt permeability, (L/m ² .h)	0.39	0.34	0.29	0.39
k, Mass transfer coefficient, (L/m ² .h)	99.00	300.00	300.00	16.09
S, Structural parameter, (μm)	564	707	1028	410
D, Diffusion coefficient, (m ² /s)	1.48 × 10 ⁻⁰⁹			

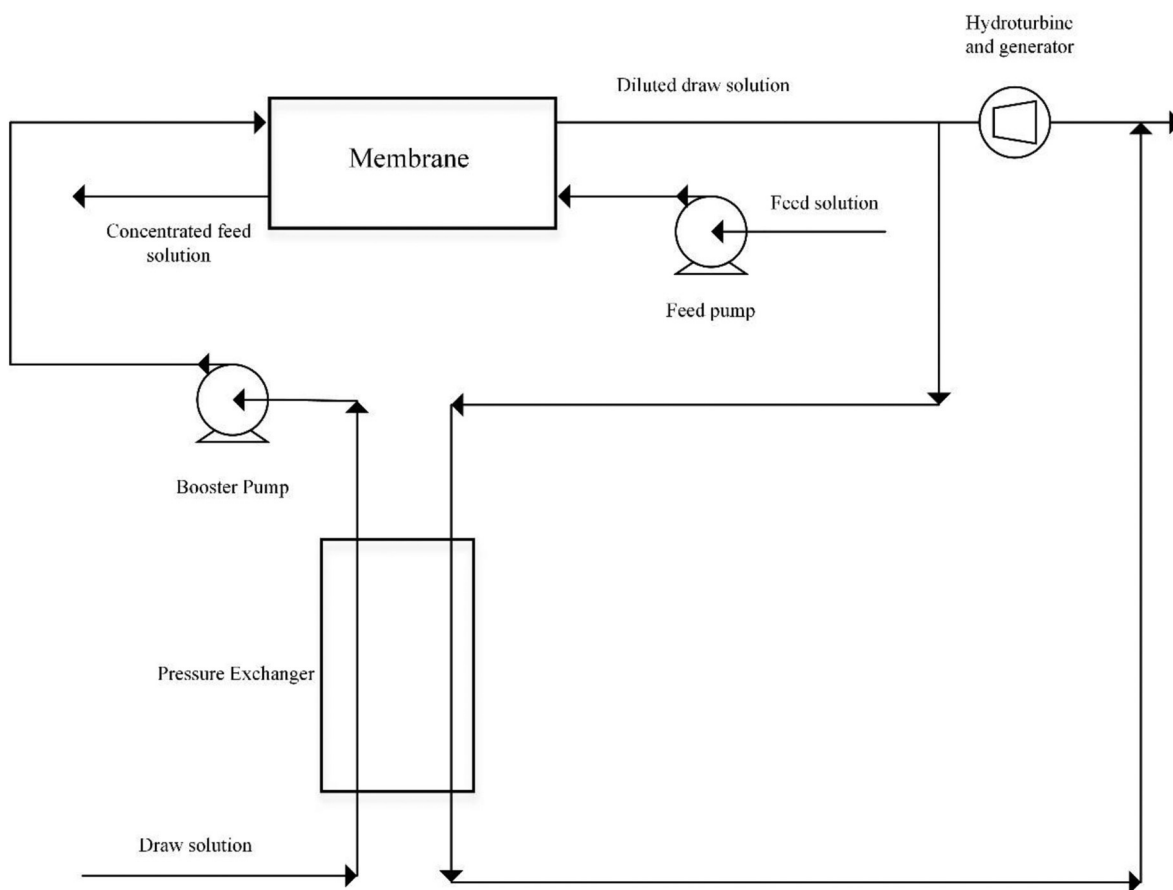


Fig. 3. PRO single-stage schematic. Figure adapted from [25].

produced water and seawater pre-treatment, a value reported for the treatment of seawater (0.08 kWh/m³) [23,24] were taken as a benchmark. Given that produced water will contain fouling agents in greater concentrations than seawater, the energetic cost of produced water treatment was assumed to be 25% greater than that of seawater (0.1 kWh/m³).

Finally, the system design chosen for this study consists of a single membrane stage - as depicted in Fig. 3. Use of the pressure exchanger maximizes the efficiency of the single-stage process. The fresh draw stream is passed through a pressure exchanger (PX) to which the energy possessed by the draw output is transferred to partially bring it up to specification pressure. The specified membrane operating pressure is then reached by feeding the partially pressurized draw stream to a booster pump before being fed into the membrane to interface with the fresh feed stream. The pressurized, diluted draw output is split such that a portion is sent to the pressure exchanger, while the remaining draw output is sent to the hydroturbine for energy recovery.

3. Results and discussion

3.1. Validation of PRO process simulator

The developed simulator is first validated against bench-scale experimental performance data for the membrane materials being investigated in this study. This ensures that observed experimental performance is borne out by the underlying mass transfer model, with the use of reported membrane characteristic parameters transferred as inputs to the simulator. Bench-scale experimental data reported by Straub et al. [4] has been satisfactorily correlated by the simulator in a previous work [8].

In addition, similar validation runs are executed in conjunction with

the experimental results reported by both Madsen et al. [3], and for the commercial PRO membrane developed by Toray. Madsen et al. [3] report dependence of the structural parameter (S) on applied pressure. To account for this, a suitable correlation to map the pressure-dependence of the structural parameter was programmed into the simulator – such that would fit experimentally-determined trends. Fig. 4 presents the pressure-dependence of the structural parameters of FTS-CTA and

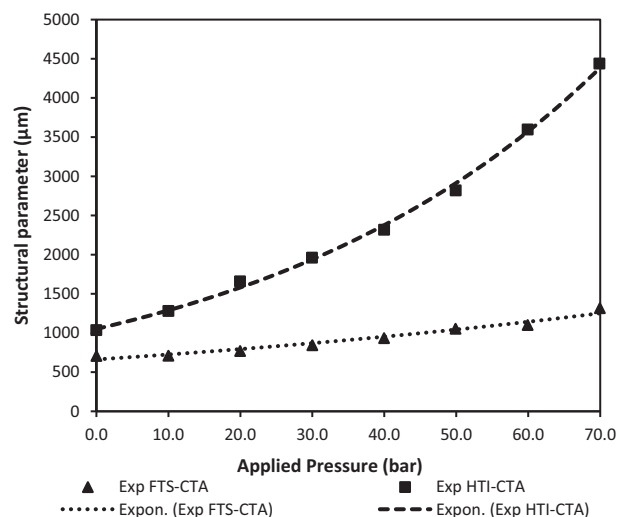


Fig. 4. Structural parameter against applied pressure for FTS-CTA and HTI-CTA membranes. 3.0 M NaCl solution used on the draw side and deionized water used on the feed side. Temperature of the system was 298.15 K. Data taken from Madsen et al. [3].

Table 2

Parameters determined after minimizing the exponential function for structural parameter dependence on applied pressure.

	m	n
FTS-CTA	662.09	0.0091
HTI-CTA	1051.2	0.0204

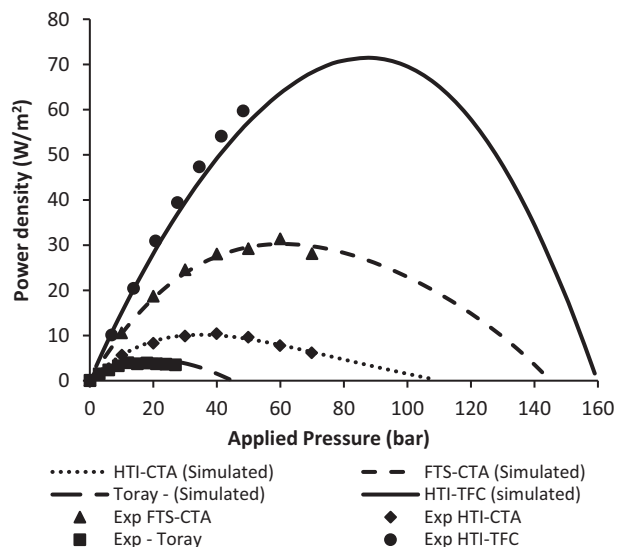


Fig. 5. Power density as a function of applied pressure for HTI-TFC, FTS-CTA, HTI-CTA and Toray membranes. 3.0 M NaCl solution used as draw and deionized water used as feed for FTS-CTA, HTI-CTA and HTI-TFC membranes. 1.0 M NaCl solution used as draw and deionized water used as feed for Toray membrane. Experimental data for FTS-CTA and HTI-CTA membranes taken from Madsen et al. [3]. Experimental data for HTI-TFC membranes taken from Straub et al. [4]. Experimental data for Toray membrane taken from Gonzales et al. [21].

HTI-CTA membrane structural parameters, respectively. The dotted lines represent the lines of best fit to model the structural parameter behavior – generated using a suitable exponential function. Eq. (23) is chosen to represent the experimental data in Fig. 4, where P represents the operating pressure and S represents the corresponding structural parameter. Parameters m and n of Eq. (23) are determined by minimizing the error between the exponential function and experimentally determined structural parameters. Table 2 presents the parameters that are determined after error minimization methodology is applied.

$$S = m e^{nP} \quad (23)$$

Fig. 5 presents simulator results for HTI-TFC, FTS-CTA, HTI-CTA and Toray membranes along with their respective experimentally determined power densities. It can be seen that the simulator is able to reliably correlate the power densities for FTS-CTA and HTI-CTA membranes – once suitable correlations of the pressure-dependence of the membrane structural parameter are programmed within the simulator.

Additional validation runs have been executed with the simulator with respect to the performance of commercial PRO membranes (Toray) – as observed experimentally by Gonzales et al. [21]. From Fig. 5, it can be observed that the simulator predicts power density with reasonable accuracy up until pressures of 10 bar with deviations beyond this point. This can likely be associated with the deformation of the membrane and no explicit treatment of the pressure-dependence of the membrane structural parameter was considered for this membrane.

It should be noted that reproducing coupon-scale PRO data will guarantee appropriate treatment for the calculation of permeate flow and average power density in a plant-scale, flat-sheet module fabricated

Table 3

Parameters studied in the optimization run.

Parameter	Limits
Draw pressure (bar)	$5 < \Delta P < 55$
Draw flowrate (m^3/h)	$0.42 < \dot{V}_D < 0.62$
Feed flowrate (m^3/h)	$0.42 < \dot{V}_F < 0.62$
Area (m^2)	$30 < A < 100$

with the same material. Correct coupon-scale calculations imply that the simulator is able to calculate permeate flux at any given point along the membrane. Total permeate flow is readily determined by numerically integrating this flux calculation along the membrane area.

3.2. Optimization results

3.2.1. Membrane 1 (HTI-TFC)

Membrane characteristic properties reported by Straub et al. [4] (presented in Table as Membrane 1) form the basis for the first plant-scale optimization study – assuming the fabrication of modules with membrane leaves of the same material characterized at the coupon-scale. The target combined feed and draw flowrate entering the plant is set to 3.0 million gallons per day (MGD), approximately $9.47 \text{ m}^3/\text{s}$. The program automates successive optimization runs of applied pressure for various combinations of pre-specified (suggested by the optimizer) flowrates and areas. The maximum applied pressure was capped at 55 bar – consistent with the burst pressure of the membrane. Ranges over which operating parameters were allowed to vary across all optimization runs are summarized in Table 3.

Results corresponding to a subset of optimization runs are used to synthesize the Pareto curve presented in Fig. 6 – explicit in specific energy and power density. The Pareto curve traces the path along which it is not possible to improve the power density without diminishing the specific recoverable energy (or vice versa), i.e. a zero-sum game. The inherent competition between power density and specific energy arises from the direct relationship between area and rate of permeation. Larger areas translate to an increase in the magnitude of recovered energy and, for a fixed total flowrate, specific energy. On the contrary, an increase in area reduces the average power density of the membrane. This can be inferred from Eq. (21) in conjunction with an understanding of dilution effects: the average power density is a direct function of the permeate flowrate divided by the area of the membrane module. Successive increases in membrane area result in diminishing marginal returns of permeated flowrate – consistent with the effect of continuous dilution of the draw stream reducing the average driving

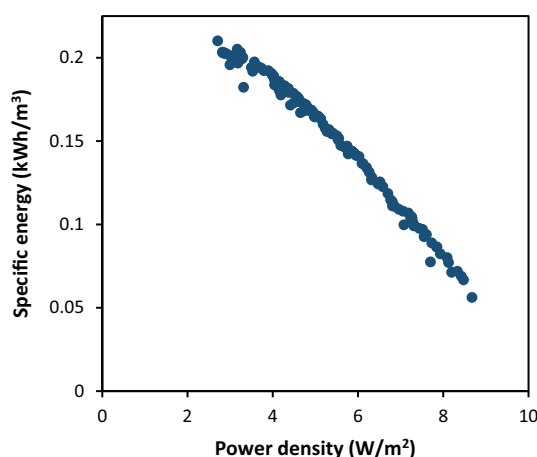


Fig. 6. Specific energy vs Power density Pareto curve for the optimization carried on Membrane 1.

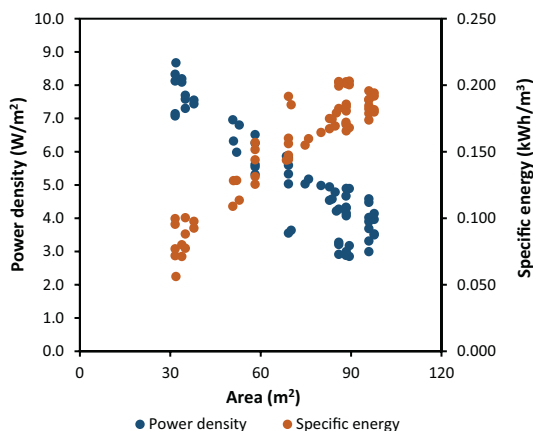


Fig. 7. Power density and Specific energy vs Area.

force across the membrane. Therefore, as area increases, the rate of change of the denominator of Eq. (21) surpasses that of the numerator – resulting in an overall net reduction in power density.

A traditional rule-of-thumb is to define an “acceptable” minimum power density at 5 W/m^2 [26]. Subsets of plant operating conditions which meet this criterion, while still resulting in optimal values for specific recoverable energy, may be identified as the region of data points in Fig. 7 which lie in the vicinity of the 5 W/m^2 threshold. Fig. 8a and b present the optimum applied hydraulic pressure differences, reduced flowrates (given by Eq. (24)) and areas which correspond to the optima which form the Pareto curve in Fig. 6. It is observed that optimum hydraulic pressures do not vary significantly from the range of 48–51 bar (approximately half the osmotic pressure difference between the feed and draw streams). Moreover, the reduced flowrate (ϕ) also varies in the range of 0.4 and 0.6. These observations are consistent with optima reported in the literature for PW-SW salinity pairings.

$$\phi = \frac{\dot{V}_F}{\dot{V}_F + \dot{V}_D} \quad (24)$$

The optimization methodology utilized for the membrane fabricated by Straub et al. [4] (i.e. Membrane 1 – HTI-TFC) is deployed for additional PRO membranes compatible with the use of high osmotic pressure difference stream pairings (due to their high burst pressures). Use of the same optimization methodology – including the development of Pareto curves with respect to power density and specific energy recovery – enables comparisons between the performance of different membranes to be made on a level playing field. Rather than simulating membranes at a common set of operating conditions, each membrane is evaluated at *membrane-specific* optima as the basis for meaningful comparisons. This approach has culminated in the generation of a set of

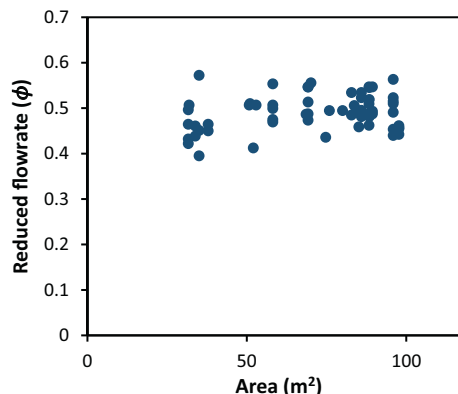
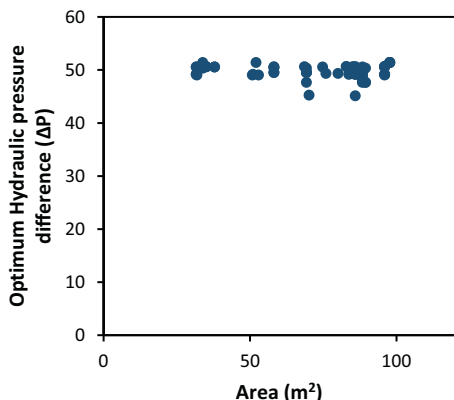


Fig. 8. Optimum hydraulic pressure difference (a) and Optimum reduced flowrate (b) vs area.

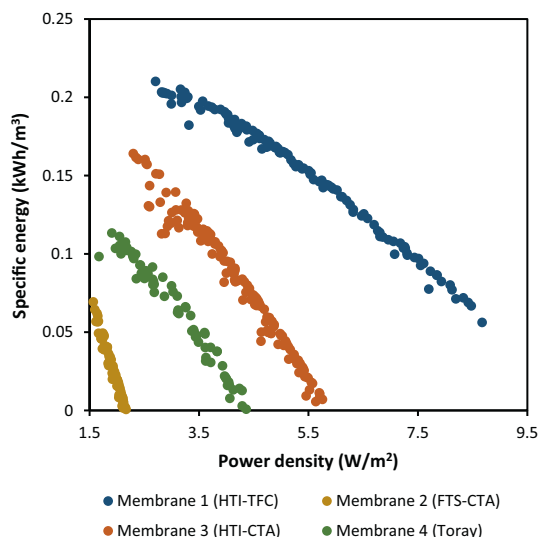


Fig. 9. Specific energy vs. power density Pareto curves for optimizations carried out on Membranes 1-4.

Pareto curves – each of which can be taken as the *performance frontier* of a given membrane i.e. the maximum achievable performance of the membrane over the optimization range. Pareto curves for Membranes 1-4 are presented in Fig. 9, and discussed in the subsequent sections.

3.2.2. Membranes 2 (FTS-CTA) and 3 (HTI-CTA)

The range of applied hydraulic pressures over which optimization runs are allowed to vary for Membranes 2 and 3 (up to 70 bar) is broader than that of Membrane 1 – consistent with their higher burst pressures. Overall, neither Membranes 2 nor 3 are able to achieve power densities and specific energies as high as those obtained from simulations on Membrane 1. This is despite the higher operating pressures (up to 70 bar) made accessible to the PRO process by the higher burst pressures of Membranes 2 and 3 – relative to that of Membrane 1 (48 bar). This can best be ascribed to the more favorable mass transfer behavior of Membrane 1 in particular, and the degradation of membrane performance (due to membrane deformation) at higher pressures in general. While select operating conditions enable Membrane 3 to demonstrate maximum power densities in the order of 5 W/m^2 , this corresponds to relatively unfavorable specific energy recoveries ($\approx 0.02 \text{ kWh/m}^3$). The estimation of membrane module payback periods (to be discussed in subsequent sections) translate these energy-explicit indicators into more useable measures of economic feasibility.

3.2.3. Membrane 4 (Toray)

In order to assess the performance of commercialized PRO membranes, the developed methodology for process optimization was additionally deployed for the performance analysis of a commercial PRO membrane (Toray) – as observed experimentally by Gonzales et al. [21] (Membrane 4). As before, the pressure range over which optimization runs are allowed to vary reflects the burst pressure of the membrane itself (in this case, 30 bar).

Membrane 4 achieves a power density vs. specific energy Pareto profile with magnitudes which are diminished relative to those of Membranes 1 and 3. This is best explained by the relatively lower burst pressure of this particular membrane – which imposes a cap on the operating pressure accessible to the process (and to the optimizer) lower than the theoretical optimum (≈ 50 bar). An exception is Membrane 2 which, though possessing a burst pressure of 70 bar, performs unfavorably relative to Membrane 4.

4. Discussion: how credible is the 5 W/m² viability threshold?

It is a common practice of researchers to specify 5 W/m² as the benchmark power density which, once demonstrated at the coupon-scale by a given membrane material, suggests its viability for plant-scale PRO. This threshold is applied generally to PRO processes [27–29] – irrespective of the selection of feed and draw stream salinities. Due to dilution effects which emerge with membrane scale-up, power densities measured at the coupon-scale are not representative of plant-scale performance. Even if dilution effects are accounted for, and it has been verified that the threshold of 5 W/m² is indeed the average power density projected to be met by the plant-scale membrane module, the results of PRO plant optimization cases examined in this work indicate that meeting this threshold is insufficient to guarantee the feasibility of the process. This is best illustrated by exploring the concept of payback period.

Pareto curves with respect to power density vs. specific energy generated for each membrane may be taken as indicative of the competing goals to recover a given unit of energy by: investing the minimum amount of membrane material (as a function of effective membrane area); utilizing a minimum total flowrate of feed and draw stream inputs to the PRO process (which factors into pumping and pretreatment costs). Specifying equipment and utility costs, one may then proceed to estimate the payback period to recover capital expenditure associated with the plant. Applicable cost parameters are summarized in Table 4.

The payback period may be calculated for each point along the Pareto curve – as presented for Membrane 1 in Fig. 10.

The minimum payback period does not necessarily coincide with process designs which maximize the power density. For Membrane 1, PRO process conditions which are collectively specified such that they minimize the payback period of the process coincide with a power density of ≈ 6.5 W/m². Greater than the rule-of-thumb threshold of 5 W/m², and less than the maximum power density achievable by the process, this result significantly casts doubt on the usefulness of specifying a threshold power density at all. Minimum payback periods for Membranes 1–4 are summarized in Table 5 – reinforcing the general observation that process designs which maximize the power density achievable by the membrane are not economically feasible from the view of recovering capital investment associated with establishing a PRO power generation plant. As indicated by the numbers for

Table 4

Cost parameter used for payback period calculation.

Parameter	Value (\$)	Reference
Cost of membrane per m ²	10	[30]
Selling price of electricity per kWh	0.036	[31]

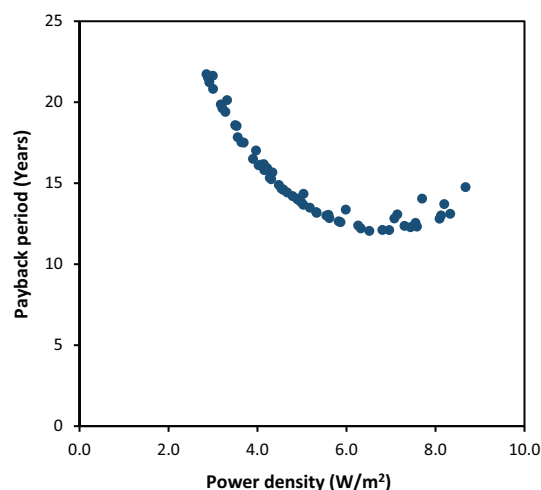


Fig. 10. Payback period as a function of power density for Membrane 1.

Membrane 3 in particular, achieving plant-scale power densities in excess of 5 W/m² does not guarantee the feasibility of the process (corresponding to payback periods exceeding 30 years). However, it should be clarified that this analysis only questions the usefulness of the 5 W/m² rule-of-thumb, or performance criteria which are based predominantly on membrane power density – without ruling out the potential feasibility of these membranes as realized through further optimization of the PRO flowsheet (e.g. staging, coupling with membrane desalination units, manipulation of feed/draw compositions etc.).

5. Conclusions

A process simulation-optimization framework was developed to evaluate the viability of high-pressure PRO membranes for energy recovery from high salinity hydrocarbon-produced water. It incorporates the use of an electrolyte equation of state for accurate osmotic pressure calculations, and mass transport models to account for performance-limiting phenomena – all integrated into a combined scheme for mass and energy balances. The results of this study conclude that application of a 5 W/m² is not sufficient to guarantee the feasibility of the membrane material in plant-scale operation – in the absence of additional optimization of the PRO process flowsheet. Instead, it is recommended to scrutinize each membrane, as defined by its characteristic mass transfer parameters, in the light of a detailed techno-economic analysis, and in conjunction with a suitable process optimization framework, as deployed in this study. By first identifying conditions which collectively enable the process to make the most out of a given membrane, it then becomes possible to draw unequivocal conclusions about the membranes' viability for PRO.

Credit Author Statement

Husnain Manzoor: Methodology, Software, Data curation, Investigation, Visualization, Writing - original draft. Muaz A. Selam: Formal analysis; Investigation; Writing - original draft. Samer Adham: Supervision, Review & editing. Ho Kyong Shon: Supervision, Review & editing. Marcelo Castier: Conceptualization, Methodology, Validation, Writing - review & editing. Ahmed Abdel-Wahab: Conceptualization, Supervision; Project administration; Resources; Funding acquisition; Writing - review & editing.

Declaration of competing interest

The authors declare that they have no known competing financial interests or personal relationships that could have appeared to

Table 5
Minimum achievable payback periods over optimization range of each membrane.

Membrane #	Minimum payback period/ yrs.	Power density associated with minimum payback period/ (W/m ²)	Maximum power density achievable within optimization constraints/ (W/m ²)
1	12.0	6.51	8.68
2	70.0	1.57	2.60
3	22.6	3.71	5.81
4	32.3	2.80	4.42

influence the work reported in this paper.

Acknowledgments

This study was made possible by a grant from the Qatar National Research Fund under its National Priorities Research Program award number NPRP10-1231-160069 and by financial support from ConocoPhillips Global Water Sustainability Center (GWSC). The paper's contents are solely the responsibility of the authors and do not necessarily represent the official views of the Qatar National Research Fund. We would like to thank ConocoPhillips Global Water Sustainability Center for funding the Graduate Assistantship position associated with this project, and for insightful discussions with their team.

References

- [1] S. Lee, J. Choi, Y.G. Park, H. Shon, C.H. Ahn, S.H. Kim, Hybrid desalination processes for beneficial use of reverse osmosis brine: current status and future prospects, *Desalination* 454 (2019) 104–111.
- [2] F.Y. Huang, A.D. Martinez, Q. Wei, Beneficial use of highly saline produced water in pressure-retarded osmosis, *Environ. Eng. Sci.* 35 (5) (2018) 472–483.
- [3] H.T. Madsen, S.S. Nissen, J. Muff, E.G. Søgaard, Pressure retarded osmosis from hypersaline solutions: investigating commercial FO membranes at high pressures, *Desalination* 420 (2017) 183–190.
- [4] A.P. Straub, N.Y. Yip, M. Elimelech, Raising the bar: increased hydraulic pressure allows unprecedented high power densities in pressure-retarded osmosis, *Environ. Sci. Technol.* 1 (1) (2014) 55–59.
- [5] Y.C. Kim, M. Elimelech, Potential of osmotic power generation by pressure retarded osmosis using seawater as feed solution: analysis and experiments, *J. Membr. Sci.* 429 (2013) 330–337.
- [6] W. Yang, L. Song, J. Zhao, Y. Chen, B. Hu, Numerical analysis of performance of ideal counter-current flow pressure retarded osmosis, *Desalination* 433 (2018) 41–47.
- [7] R. Long, X.T. Lai, Z.C. Liu, W. Liu, Pressure retarded osmosis: operating in a compromise between power density and energy efficiency, *Energy* 172 (2019) 592–598.
- [8] H. Manzoor, M.A. Selam, F.B. Rahman, S. Adham, M. Castier, A. Abdel-Wahab, A tool for assessing the scalability of pressure-retarded osmosis (PRO) membranes, *Renew. Energy* 149 (2020) 987–999.
- [9] R. Soltani, H. Struchtrup, Modeling and simulation of the dual stage pressure retarded osmosis systems, *Desalination* 460 (2019) 28–40.
- [10] K. Touati, J. Salamanca, F. Tadeo, H. Elfil, Energy recovery from two-stage SWRO plant using PRO without external freshwater feed stream: theoretical analysis, *Renew. Energy* 105 (2017) 84–95.
- [11] A. Zuber, R.F. Checoni, M. Castier, Thermodynamic properties of aqueous solutions of single and multiple salts using the Q-electrolattice equation of state, *Fluid Phase Equilib.* 362 (2014) 268–280.
- [12] A. Zuber, R.F. Checoni, R. Mathew, J.P.L. Santos, F.W. Tavares, M. Castier, Thermodynamic properties of 1:1 salt aqueous solutions with the electrolattice equation of state, *Oil Gas Sci. Technol.* 68 (2) (2013) 255–270.
- [13] M. Born, Volumen und hydrationswärme der ionen, *Z. Phys.* 1 (1) (1920) 45–48.
- [14] L. Blum, Mean spherical model for asymmetric electrolytes: I. method of solution, *Mol. Phys.* 30 (5) (1975) 1529–1535.
- [15] S. van der Zwan, I.W. Pothof, B. Blankert, J.I. Bara, Feasibility of osmotic power from a hydrodynamic analysis at module and plant scale, *J. Membr. Sci.* 389 (2012) 324–333.
- [16] N.Y. Yip, A. Tiraferri, W.A. Phillip, J.D. Schiffman, L.A. Hoover, Y.C. Kim, M. Elimelech, Thin-film composite pressure retarded osmosis membranes for sustainable power generation from salinity gradients, *Environ. Sci. Technol.* 45 (10) (2011) 4360–4369.
- [17] F.P. Miller, A.F. Vandome, J.U.h.b.g.c.q.b.i.M.Q. McBrewster, *Bernoulli's Principle*, Alphascript Publishing, 2010.
- [18] N. Denko, <https://www.lenntech.com/products/Hydranautics-SWC-Membranes/SWC4B-MAX-8040/SWC4B-MAX-8040/index.html>, (2019), Accessed date: 12 October 2019.
- [19] Y.C. Kim, Y. Kim, D. Oh, K.H. Lee, Experimental investigation of a spiral-wound pressure-retarded osmosis membrane module for osmotic power generation, *Environ. Sci. Technol.* 47 (6) (2013) 2966–2973.
- [20] K. Lee, R. Baker, H. Lonsdale, Membranes for power generation by pressure-retarded osmosis, *J. Membr. Sci.* 8 (2) (1981) 141–171.
- [21] R.R. Gonzales, M.J. Park, T.H. Bae, Y.Q. Yang, A. Abdel-Wahab, S. Phuntsho, H.K. Shon, Melamine-based covalent organic framework-incorporated thin film nanocomposite membrane for enhanced osmotic power generation, *Desalination* 459 (2019) 10–19.
- [22] B.M. Adams, L.E. Bauman, W.J. Bohnhoff, K.R. Dalbey, M.S. Ebeida, J.P. Eddy, M.S. Eldred, P.D. Hough, K.T. Hu, J.D. Jakeman, J.A. Stephens, L.P. Swiler, D.M. Vigil, T.M. Wildey, Dakota, a multilevel parallel object-oriented framework for design optimization, parameter estimation, uncertainty quantification, and sensitivity analysis: version 6.0 User's manual, Sandia Technical Report SAND2014-4633, July 2014.
- [23] T. Al-Sarkal, H.A. Arafat, Ultrafiltration versus sedimentation-based pretreatment in Fujairah-1 RO plant: environmental impact study, *Desalination* 317 (2013) 55–66.
- [24] A.P. Straub, A. Deshmukh, M. Elimelech, Pressure-retarded osmosis for power generation from salinity gradients: is it viable? *Energy Environ. Sci.* 9 (1) (2016) 31–48.
- [25] H. Manzoor, Texas A & M University (Ed.), *Simulation of Full-Scale Pressure Retarded Osmosis Processes*, Master's Thesis, 2019.
- [26] S.E. Skilhagen, J.E. Dugstad, R.J. Aaberg, Osmotic power—power production based on the osmotic pressure difference between waters with varying salt gradients, *Desalination* 220 (1-3) (2008) 476–482.
- [27] A. Altaee, A. Cipolina, Modelling and optimization of modular system for power generation from a salinity gradient, *Renew. Energy* 141 (2019) 139–147.
- [28] Q. She, X. Jin, C.Y. Tang, Osmotic power production from salinity gradient resource by pressure retarded osmosis: effects of operating conditions and reverse solute diffusion, *J. Membr. Sci.* 401 (2012) 262–273.
- [29] F. Helfer, C. Lemckert, Y.G. Anissimov, Osmotic power with pressure retarded osmosis: theory, performance and trends—a review, *J. Membr. Sci.* 453 (2014) 337–358.
- [30] I.L. IndiaMart, <https://www.indiamart.com/proddetail/dow-hsro-4040ff-21884813262.html>, (2020), Accessed date: March 2020.
- [31] KAHARAMAA, <https://www.km.qa/CustomerService/Pages/Tariff.aspx>, (2020), Accessed date: March 2020.